



## Full Text View

[Volume 32, Issue 2 \(February 2002\)](#)

### Journal of Physical Oceanography

Article: pp. 585–598 | [Abstract](#) | [PDF \(1.02M\)](#)

# Coherent Eddies in the Labrador Sea Observed from a Mooring

**Jonathan M. Lilly and Peter B. Rhines**

*School of Oceanography, University of Washington, Seattle, Washington*

(Manuscript received February 17, 2000, in final form January 23, 2001)

DOI: 10.1175/1520-0485(2002)032<0585:CEITLS>2.0.CO;2

### ABSTRACT

During June–November 1994, a mooring in the central Labrador Sea near the former Ocean Weather Station Bravo recorded a half-dozen anomalous events that prove to be two different types of coherent eddies. Comparisons with simple analytical models are used to classify these events as coherent eddies on the basis of their velocity signatures. The first clear examples of long-lived convectively generated eddies are reported. These four small (radius  $\sim 5$ – $15$  km) eddies are exclusively anticyclonic, with cold, fresh middepth potential temperature ( $\theta$ ) and salinity ( $S$ ) cores surrounded by azimuthal currents of  $\sim 15$  cm s $^{-1}$ . Their  $\theta/S$  properties identify them unambiguously as the products of wintertime deep convection in the interior Labrador Sea. Compared with eddies in other regions, these anticyclones are unusual for their strong surface expressions and composite  $\theta/S$  cores. Two warm cyclones are also seen; these are larger (radius  $\sim 15$  km) than the anticyclones and about as energetic (currents  $\sim 15$  cm s $^{-1}$ ). Their  $\theta/S$  and potential vorticity properties suggest that they are created by stretching a column of water from the Irminger Current, which surrounds the Labrador Sea on three sides.

### 1. Introduction

The coherent eddy field plays an important role in convective regions such as the Labrador Sea. Baroclinic, property-carrying eddies are expected to mediate the dispersal of convected water from a well-convected patch into the ambient sea ([Legg and Marshall 1993](#); [Send and Marshall 1995](#)), as well the restratification of the water column following deep convection ([Jones and Marshall 1997](#)). Convectively generated deformation-scale eddies have been observed in the Labrador Sea using floats and hydrography by [Gascard and Clarke \(1983\)](#). However, direct measurements of the effects of such eddies, in the Labrador Sea or elsewhere, remain elusive ([Marshall and Schott 1999](#), 107–108). Coherent eddies may be important to deep convection in another way: cyclonic eddies

#### Table of Contents:

- [Introduction](#)
- [Data and methods](#)
- [Eddylike events in the](#)
- [Kinematic models of eddy](#)
- [Structure of observed](#)
- [Discussion](#)
- [REFERENCES](#)
- [APPENDIX](#)
- [TABLES](#)
- [FIGURES](#)

#### Options:

- [Create Reference](#)
- [Email this Article](#)
- [Add to MyArchive](#)
- [Search AMS Glossary](#)

#### Search CrossRef for:


- [Articles Citing This Article](#)

#### Search Google Scholar for:


- [Jonathan M. Lilly](#)
- [Peter B. Rhines](#)

can destabilize the upper water column, “preconditioning” it for deep convection ([Legg et al. 1998](#); [Straneo and Kawase 1999](#)).

The Labrador Sea, the site of deep convection reaching a depth of over 2 km during some winters, is of particular importance for its influence on the  $\theta/S$  and potential vorticity structure of the North Atlantic ([Talley and McCartney 1982](#)) and as a potentially sensitive location for the thermohaline circulation ([Häkkinen 1999](#)). Convection there has long been known to account for both annual and interannual variations in the water-mass properties ([Lazier 1973, 1980](#)) and to involve organizations across a range of scales, from submesoscale to basin-scale ([Clarke and Gascard 1983](#); [Gascard and Clarke 1983](#)).

For these reasons a long-term mooring, located at 56.75°N, 52.5°W ([Fig. 1](#) ) near the site of the former Ocean Weather Station (OWS) Bravo, was established to monitor interannual variability in the central Labrador Sea. The present work is the second involving the Bravo mooring; the first ([Lilly et al. 1999](#), hereafter [LS99](#)) described one annual “cycle” of  $\theta/S$  properties and currents for the year June 1994–June 1995. Here we focus on the nonconvecting period June–November 1994 to develop methods for investigating the structure of coherent eddies from a mooring.

## 2. Data and methods

The data used for this paper were described in detail in [LS99](#), but we will summarize here. The primary data (see [Table 1](#) ) are from six SeaBird SBE 16 SEACATs measuring temperature and conductivity, and six Aanderaa RCM-8 instruments measuring current speed and direction as well as temperature, all sampling at hourly intervals. Pressure was measured at two instruments, allowing us construct a pressure record at all depths through the use of a mooring model. All temperature data were recast into potential temperature, using a fixed salinity profile for those instruments that lacked salinity. Temperature and salinity data were calibrated against endpoint CTD casts.

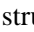
The inertial wave/semidiurnal tidal band has an amplitude of typically 5 cm s<sup>-1</sup> (10 cm s<sup>-1</sup> peak-to-peak) and so is a signal roughly half the magnitude of that due to the eddies. All time series are therefore filtered with a 24-h Hanning filter; this length filter was found to be the best compromise between removing tidal noise and keeping high-frequency fluctuations due to eddies.

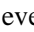

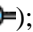

The density signal of the eddies is small and very sensitive to choice of reference level. At each instrument we define a quantity

$$\sigma_L = \rho(s, t, p, \bar{p}) \quad (1)$$

where  $\bar{p}$  is the average instrument pressure, which we refer to as the locally referenced potential density. Another useful quantity is the isopycnal displacement  $\Delta Z_\sigma$ , which we find by interpolating  $\sigma_L$  within a vertical profile derived from CTD data. This is useful for comparisons across different depths, but has a high noise level in the central water column owing to the weak stratification.

## 3. Eddylike events in the mooring data

The flow in the interior Labrador Sea (see [LS99](#)) is nearly barotropic and highly variable. For the June–November 1994 period that this paper focuses on, the magnitude of the mean vertically averaged current is 4.1 cm s<sup>-1</sup> to the southwest, and its standard deviation is 11.4 cm s<sup>-1</sup>. Over 90% of the energy can be accounted for by the barotropic mode. Departures from barotropic flow are found not only in the upper water column but also and primarily in the lowest kilometer. This shear structure reflects the stratification ([Figs. 2, 3](#) ) , which consists of the weakly stratified Labrador Sea Water (LSW) between about 500 and 2000 m depth sandwiched between a ~ 500 m thick stratified layer at the surface and an ~ 1 km stratified layer at the bottom. The linear, flat-bottom vertical modes computed from the CTD data show that the first baroclinic mode has the upper 2 km and lower 1 km out of phase, with a corresponding deformation radius of 7 km. This mode dominates the baroclinic signal in the mooring data.

The currents measured during June–November 1994 in the central water column contain a number of sudden rotational events, seen in a stick-vector plot ([Fig. 4a](#) ) and especially in the time series of  $u$  and  $v$  ([Fig. 4b](#) ) . These transitions in the velocity field tend to be associated with extrema of the isopycnal displacement observed at 2500 m (and other depths), as well as with upper-level temperature anomalies ([Figs. 4c,d](#) ) ; similar depressions of the deep stratification associated with  $\theta/S$  anomalies are occasionally observed in the CTD data ([Fig. 2](#) ) . Six events (A–F) are marked, each of which has a temperature anomaly (anywhere in the water column) greater than 0.05°C, an isopycnal displacement magnitude greater than 100 m, and a velocity anomaly greater than 10 cm s<sup>-1</sup>; no other events during this time period meet all three criteria. We will argue that these six events are advected eddies.

Vertical–temporal “slices” through each of these events (Fig. 5) reveal eddylike structures, with a middepth  $\theta/S$  core surrounded by a ring of strong currents. Here the velocity has been rotated into components ( $u_p, \mathbf{v}_n$ ) parallel to and normal to the estimated advecting flow, with the normal component  $\mathbf{v}_n$  shown. As discussed in the following section, the dominant signal of an advected eddy is expected to be in the normal component, with  $\mathbf{v}_n$  initially positive (negative) for a cyclone (anticyclone). Events C and D thus appear to be cyclonic eddies, while the others are anticyclones.

Figure 6 shows the hodograph (the curve traced out by the tip of the velocity vector with time) and its integral, the progressive vector diagram, for the velocity time series shown in Figs. 4a and 4b. The shading is the potential temperature at 1010 m, detrended to remove a slow warming. The six events A–F are all associated with a  $10 \text{ cm s}^{-1}$  or larger turning of the velocity vector, the edges of which coincide with the edges of a temperature anomaly. Within the temperature anomaly the hodograph tends to be relatively straight, and on either side are found regions having the opposite rotation sense from the central region. The progressive vector diagram has bends at the locations of these events, with bends to the right (left) associated with the apparent cyclones (anticyclones).

The vertical slices as well as the temporal structure of the currents support the diagnosis of these six events as advected coherent eddies. This argument is strengthened by comparison with analytical models in the following section. Some readers may wish to turn immediately to the physical description of events A–F given in section 5.

#### 4. Kinematic models of eddy advection

Inferring the two-dimensional ( $x, y$ ) nature of an event based on its ( $u, \mathbf{v}$ ) signature at a single point is inherently complicated and warrants a careful examination of the expected currents due to an advected eddy and other basic structures.

##### a. An isolated eddy

Let an eddy be advected by a spatially uniform but time-varying flow  $\mathbf{U}(t) + i\mathcal{V}(t)$  so that the eddy's trajectory can be represented by a curve on the complex plane

$$\boldsymbol{\eta}(t) \equiv r'(t)e^{i\phi(t)} \equiv x'(t) + iy'(t) = \int \mathbf{U} + i\mathcal{V} dt.$$

The currents observed by a mooring at the origin are

$$\boldsymbol{\xi}(t) \equiv \mathbf{U} + i\mathcal{V} - ie^{i\phi}\bar{\mathbf{v}}(r')$$

and the currents due to the eddy only are

$$\boldsymbol{\xi}'(t) \equiv \boldsymbol{\xi} - (\mathbf{U} + i\mathcal{V}) = -ie^{i\phi}\bar{\mathbf{v}}(r'), \quad (2)$$

where  $\bar{\mathbf{v}}(r)$  describes the radial velocity profile of this (azimuthally symmetric) eddy and is positive for cyclonic currents. Equation (2) states that an eddy's trajectory, modified by the azimuthal velocity profile, traces out the currents observed at a mooring. The magnitude of the eddy currents is simply given by the distance from the mooring to the eddy center  $r'(t)$  through the azimuthal velocity profile as

$$|\boldsymbol{\xi}'(t)| = |\bar{\mathbf{v}}(r'(t))|.$$

The orientation of the eddy currents is given by rotating  $\boldsymbol{\eta}$ , the line from the mooring location to the eddy center, 90 degrees counterclockwise through the factor  $-ie^{i\phi(t)}$ . An obvious but surprisingly useful consequence of (2) is that the eddy currents are always perpendicular to  $\boldsymbol{\eta}$ .

A very simple model eddy consists of solid-body rotation within a core ( $r < R$ ) and  $1/r$  decay elsewhere,

$$\bar{\mathbf{v}}(r) = \begin{cases} VrR^{-1}, & r < R \\ VRr^{-1}, & r > R, \end{cases} \quad (3)$$

and is known as the Rankine vortex. Here  $V$  is the maximum azimuthal velocity (positive for a cyclone). If the flow is in

quasigeostrophic balance, the Rankine vortex is advected to a uniform potential vorticity (PV) anomaly within radius  $R$  of magnitude  $q = 2V/R$ .

The currents observed by a north–south array of moorings as a Rankine vortex is advected past by a constant eastward flow  $U$  (Fig. 7) are even in the parallel (eastward) direction and odd in the normal (northward) direction. The resulting hodographs (Fig. 7b) are straight lines when the mooring is inside the eddy core and circles when the mooring is outside the core. The ends of the hodograph return to the value of the mean flow as the distance to the eddy center becomes large. For “slices” that intersect the eddy core, the combination of a straight line with a segment of a circle results in a “D” shape with the flat part of the “D” perpendicular to the advecting flow. The nearer the slice to the center of the eddy, the more the hodograph collapses onto a straight line.

The reasons for the straight lines and circles can be seen by considering (2) for the specific case of a Rankine vortex, which becomes

$$\xi'(t) = \begin{cases} -iR^{-1}V\eta, & |\eta| < R \\ -i\eta^*{}^{-1}VR, & |\eta| > R. \end{cases} \quad (4)$$

In the interior of the Rankine vortex, the eddy velocity vector  $\xi'$  is simply the displacement vector  $\eta$  rotated 90 degrees clockwise and rescaled by a constant. Solid-body rotation therefore maps a straight line on the  $(x, y)$  plane onto a perpendicular straight line on the  $(u, v)$  plane. In particular, for an eddy advected by a constant eastward flow  $U$  the eddy location  $\eta$  is

$$\eta = x' + iy' = U(t - t_0) + id,$$

so that the  $x$  location of the eddy center is linear with time and the  $y$  location (denoted  $d$ ) is constant. It follows from (4) that

$$\xi' = u' + iv' = R^{-1}Vd - iR^{-1}VU(t - t_0)$$

so that  $u'$  is constant and  $v'$  is linear with time, as can be seen in Figs. 7c,d. Outside of the eddy's core,  $\bar{v} \sim r^{-1}$ , and basic complex analysis applied to (4) shows that a straight line  $\eta = U(t - t_0) + id$  maps onto a circle of diameter  $|d^{-1}VR|$  touching the point  $U + 0i$ .

### b. Other features

The D-shaped structures on the hodograph plane reflect the two-dimensional  $(x, y)$  structure of the eddies. By contrast the advection of a feature that is invariant in one dimension, such as a front or a filament, will result in a straight line on the  $(u, v)$  plane, as with the case of an eddy sliced through its exact center. Since a front can have any orientation with respect to the advecting flow, this straight line on the  $(u, v)$  plane need not be perpendicular to  $\mathcal{U} + i\mathcal{V}$ . Hodographs due to curved filaments are complicated (because a strongly curved filament will tend to be intersected twice) and bear little resemblance to those in Fig. 6; neither do the hodographs of a front or filament advected by an oscillatory flow. In general it seems difficult for fronts or filaments to result in hodographs similar to those of advected eddies sliced off-center.

Different velocity profiles  $\bar{v}(r)$  will, obviously, result in different hodographs, but the differences are not dramatic. For an eddy that has a radial velocity profile proportional to  $(r/R)^m$  for  $m \neq 1$  the solid-body line will become deformed, and will bow inward for  $m > 1$  or outward for  $m < 1$ . Using a Gaussian streamfunction profile, which corresponds to a more diffuse core than the observations, results in more gently curving hodographs and an outward bowing of the solid-body line. Similarly, a two-layer model with a PV anomaly in the upper layer only (using realistic parameters for the Labrador Sea) results in a more rapid ( $\propto r^{-1}$ ) decay rate outside of the core, but for deformation-scale eddies the hodographs are virtually unchanged.

The hodographs for a self-advecting dipole (not shown) are similar to those of an advected monopolar eddy only when the dipole is sliced near the location of one of its vorticity cores and when the background flow is negligible. When a dipole is sliced in between the two cores, the result is an impulsive feature: the currents suddenly accelerate and then decelerate, with the amount of rotation decreasing as the location of the slice approaches the centerline of the dipole. In general, a dipole will propagate at an angle to the advecting flow due to its self-advection, leading to “tilted” hodographs that are perpendicular to the direction of net propagation rather than to the advecting flow. Event C has a tilted hodograph that may be due to a self-advecting component. Since the other eddies observed at the mooring appear to be associated with an  $O(10 \text{ cm s}^{-1})$  advecting flow but their solid-body lines are not tilted, these features are not consistent with strongly self-advecting dipoles.

### c. An eddy field

The data resemble the model in that roughly straight-line regions of the hodographs perpendicular to the apparent background flow (with the exception of event C) are associated with temperature anomalies. The most noticeable difference between the data and the constant advecting flow model is that in the data the hodographs often do not “close” completely.

In the central Labrador Sea the assumption of a constant advecting flow is clearly unrealistic. An alternate model is a field of Rankine vortices. As a first approximation an eddy is assumed to be advected by the net velocity felt at its exact center, as in a point vortex model. Eddies of similar size and strength, plus a small random component, are initially placed on a grid, again plus a random offset. An example of a hodograph and progressive vector diagram resulting from this model is shown in [Figs. 8a and 8b](#) (see caption for model details). Hodographs no longer decay to a fixed point, but can in general be “open” or “closed.” The appearance of eddies in the eddy-field model can be qualitatively very similar to events A–F. Hodographs can therefore be easily deformed through the presence of other eddies or perhaps by other low-frequency flow components into features like those observed at the mooring.

## 5. Structure of observed eddies

In the previous sections we argued that six major events of June–November 1994 were advected coherent eddies. We now describe them in greater detail.

Estimating the structure of a coherent eddy from a mooring is inherently difficult, so our description will be limited to the relatively simple measures. The estimated eddy current strength is  $\bar{V}$  and its estimated “apparent radius” is  $\bar{X}$  where  $X$  is the half-width of the eddy chord intersected by the mooring; from these a Rossby number,

$$\mathcal{R} = \frac{2|\bar{V}|}{\bar{X}f},$$

can be formed. Details are discussed in the appendix. Estimates of other important quantities, such as the Burger number or the vorticity, are likely to be of poor quality and will not be used.

### a. Cyclones and anticyclones

The basic structures of the six observed eddies are summarized in [Table 2](#). The four anticyclonic eddies (A, B, E, F) are all similar to each other. All have middepth lenses of cold, fresh water, around which currents of 10–15 cm s<sup>-1</sup> swirl in an anticyclonic sense. The flow extends from the top instrument at 110 m to more than 2500 m for all four eddies.

Isopycnals bow out around the  $\theta/S$  cores by 150–300 m, with corresponding density anomalies of 0.01–0.02 g kg<sup>-1</sup>. The  $\theta/S$  cores are localized between  $\sim 250$  and  $\sim 1250$  m, with a maximum temperature anomaly (relative to ambient fluid) of typically  $-0.1^\circ\text{C}$  at around 500–750 m. Their properties are in the approximate range  $\theta \sim 2.6$ – $2.7$ ,  $S \sim 34.81$ – $38.82$  psu. Eddies B, E, and F have apparent radii  $X$  of roughly 5 km so that their true radii are probably comparable to the deformation radius of 7 km, while eddy A is much larger ( $X \sim 15$  km).

A trapping of the eddy currents in the upper 2.5 km appears to be a general feature of the four anticyclones, with no detectable signal of the eddy currents at the bottom current meter (3476 m). The strong isopycnal depression (see [Fig. 4c](#)) of the stratified lower layer beneath the eddy core apparently cancels the anticyclonic flow before it reaches the bottom. Associated strong density minima (0.015–0.025 kg m<sup>-3</sup>) observed at 2500 m therefore appear to be a good indication of small-scale anticyclonic eddy activity in the upper layer. In the 1994 CTD section ([Fig. 2](#)), two cusplike depressions of the deep stratification associated with fresh anomalies are probably profiles through cold eddies like those observed at the mooring. The other cusplike depressions with no  $\theta/S$  anomalies may also be due to nearby anticyclones. Similar features are observed in other years.

Rossby number estimates for the anticyclones span the range from  $\mathcal{R} \sim 0.1$  to  $\mathcal{R} \sim 0.5$ , with the two best-observed events (B and F) having relatively high Rossby numbers (0.25–0.5).

Events C and D are similar to each other in that they both have warm, salty  $\theta/S$  anomalies and cyclonic currents. However, event C has a large surface-trapped bowl of warm, salty water, whereas event D has only a weak and patchy  $\theta/S$  anomaly. These do not match the eddy-advection model as well as the anticyclones. In particular, the tilted hodograph of eddy C could mean that it is part of a self-advecting dipole, and therefore the size estimate (assuming advection) could be an underestimate. Unlike the anticyclones, they both have significant flow at the bottom. They are at least 12–20 km radius, substantially larger than the deformation radius of 7 km, with currents of 10–15 cm s<sup>-1</sup>. Rossby numbers are lower than for



the anticyclones, in the range  $\mathcal{R} \sim 0.1\text{--}0.2$ , owing to the cyclones' larger size.

### b. $\theta/S$ properties and origin

The  $\theta/S$  properties of the cold anticyclones are shown in Fig. 9a (●), together with CTD profiles from the central Labrador Sea during May/June 1994 and the one-standard-deviation envelope of mooring  $\theta/S$  variability during June–November 1994. The cores of the cold eddies contain water that is significantly colder (by  $\sim 0.05\text{--}0.1^\circ\text{C}$ ) and fresher (by  $\sim 0.01\text{--}0.02$  psu) than the ambient water. These properties do not match any other water masses in the North Atlantic since LSW is already colder and fresher along isopycnals than surrounding water masses. However, Labrador Sea Water itself undergoes an annual cycle in  $\theta/S$  properties (Lazier 1980; LS99). The coldest, freshest waters observed at a given depth occur as the convective mixed layer passes that depth, typically in February–March for depths greater than 500 m. After deep convection, the water column becomes warmer and saltier along isopycnals (by  $0.2^\circ$  at 500 m between June and December 1994), apparently due to mixing with warm, salty water from the Irminger Current (LS99). Although we have no observations of  $\theta/S$  properties during March 1994, the  $\theta/S$  properties from March 1995 were probably comparable (based on one-dimensional mixing applied to the partly restratified May–June CTD sections) and are cold and fresh enough to account for the  $\theta/S$  properties of the eddies. Therefore, it seems clear that the eddies contain convected water that has been insulated from the isopycnal warming and salinization experienced by the rest of the Labrador Sea. Assuming the eddies were formed around March 1994, we infer that eddies A, B, E, and F are about 3, 4, 5, and 8 months old, respectively.

The  $\theta/S$  diagram for the warm cyclones (Fig. 9b (●)) shows that these eddies are warmer, saltier, and less dense than the surrounding water, by  $\sim 0.1\text{--}0.2^\circ\text{C}$ ,  $\sim 0.05\text{--}0.1$  psu, and  $\sim 0.02\text{--}0.04$  g kg $^{-1}$  at  $\sim 500$  m. CTD casts are also shown from stations in the Irminger boundary current on the Greenland side of the AR7W line. The warm eddies are in between the  $\theta/S$  extremes of the boundary current core and the Labrador Sea interior, and have identical properties to water from the offshore edge of the Irminger Current. In contrast, the North Atlantic Current (to the southeast of the Labrador Sea) contains much more buoyant water, with temperatures within the same isopycnal band far higher ( $0.5^\circ$  or more) than those associated with the warm eddies.

A local origin in the Irminger Current is also consistent with the potential vorticity structure of the warm eddies. Conservation of potential vorticity states

$$\frac{\zeta_f + f_f}{h_f} = \frac{\zeta_i + f_i}{h_i}, \quad (5)$$

where  $h$  is the thickness of an isopycnal layer,  $\zeta$  is the vertical relative vorticity, and subscripts  $i$  and  $f$  denote the initial and final states of the eddy. The initial large-scale relative vorticity is negligible relative to  $f$  (assuming an  $80$  cm s $^{-1}$  shear over  $50$  km). The relative vorticity of the end state can be estimated, assuming solid-body rotation, as  $\zeta_f = 2VR^{-1} = \mathcal{R}f_f$  or  $0.1\text{--}0.2f_f$ . For eddies generated nearby  $f$  is approximately constant, and we can rewrite (5) as

$$\frac{h_f - h_i}{h_i} = \mathcal{R}, \quad (6)$$


which means the cyclonic eddies could be explained by a 10%–20% stretching. The warm eddies have  $\theta/S$  anomalies along isopycnals to a depth of 2000 m (Fig. 9b (●)), so the appropriate isopycnal range is between  $\sigma_{1.5} = 34.69$  and about  $\sigma_{1.5} = 34.63$ . The thickness between these isopycnals increases by about 40% from the boundary current (Fig. 2 (●)) to the warm eddies observed at the mooring, which is more than sufficient to account for the observed relative vorticity.

### c. Detailed structure of an anticyclone

Since eddy F was fortuitously sliced close to its center, we are able to look at the structure of this event in greater detail. The vertical structure of the currents and isopycnal displacements associated with eddy F are shown in Figs. 10a–d (●). As mentioned previously, the flow is nonzero, even at the sea surface, but a middepth maximum is obvious. However, isopycnal displacements decay to zero before reaching the surface; that is, there are no outcrops associated with the anticyclone. The anticyclonic flow observed near the surface must therefore be due to an uplift of the sea surface; the same is true for the other anticyclones.

The magnitude of the sea surface displacement can be inferred from the momentum equations. The  $x$ -integrated  $x$ -momentum equation for an azimuthally symmetric feature located at the origin is

$$p'(x) = \rho_o \int_0^x \left( f v + \frac{v^2}{x'} \right) dx', \quad (7)$$

where  $p'$  is the departure of the pressure field from the motionless hydrostatic state. The estimated advecting flow speed can then be used to substitute  $U|t - t_o|$  for  $x$ . We find it is necessary to subtract away the strongly low-passed (240 h) current at each depth so that the pressure signal due to the eddy alone can be isolated from its surroundings. The cyclostrophic term  $v^2/r$  is important only within about 1/4 radius from the eddy center ([Figs. 10e,f](#) ) , where it amounts to about a 15% correction to the geostrophic term  $fv$ . The pressure field is somewhat narrower but stronger at middepths, with the 110- and 2500 m pressure fields approximately equal in size and magnitude. The magnitude of the high pressure region at the surface (100 Pa) is equivalent to a 1 cm elevation of the sea surface.


The  $\theta/S$  core of eddy F is not a single lens but has a composite structure.<sup>1</sup> The maximum currents are associated with a  $\theta/S$  lens near 1 km, above and beneath which there are other  $\theta/S$  anomalies. No  $\theta/S$  anomaly is observed at 1.5 km, but at 2 km a lens with  $\theta/S$  properties and density similar to the main lens is observed. Higher in the water column, a third lens of very different  $\theta/S$  properties is observed, with no distinct velocity extremum. Its freshness and low density make it unlikely to have originated in the interior Labrador Sea. More likely, it is convectively modified boundary current water. Two other anticyclonic eddies (A and B) show similar, though less pronounced, composite structures.

#### d. Comparison of the anticyclones with other eddies

To the best of our knowledge, long-lived convectively formed eddies have not previously been reported, either in the Labrador Sea or elsewhere. Deformation-scale anticyclones have been observed during active convection in the Labrador Sea ([Gascard and Clarke 1983](#)), and it is possible that such eddies eventually evolve into the anticyclonic eddies we observed 3–8 months following the end of deep convection. Similarly eddies of both signs have been observed during active convection in the Mediterranean Sea ([Gascard 1978](#)).

The Labrador Sea anticyclones appear to be an example of a “submesoscale coherent vortex” (SCV) as defined by [McWilliams \(1988\)](#). In a comparison of a number of different SCVs from [D'Asaro et al. \(1994\)](#), the range of Rossby numbers for three meddies and two hydrothermal megaplumes is  $\sim 0.2$ – $0.6$ , while the two Arctic Ocean eddies reported have Rossby numbers greater than  $0.6$ . The range of estimated Rossby numbers for the cold Labrador Sea eddies ( $0.1$ – $0.5$ ) makes the anticyclones more similar to meddies and to hydrothermal megaplumes than to Arctic Ocean eddies. This perhaps reflects a common origin: meddies, hydrothermal megaplumes, and Labrador Sea anticyclones are most likely all collapse events of some kind, whereas the Arctic eddies may be generated through lateral friction ([D'Asaro 1988](#)).

One distinguishing feature of the anticyclonic eddies is their strong surface expression. The exact magnitude of the surface expression of other coherent eddies is still a matter of debate, but a survey of some meddy literature ([Riser et al. 1986](#); [Elliott and Sanford 1986](#); [Käse and Zenk 1987](#); [Stammer et al. 1991](#)) suggests that an upper bound on the ratio of surface to maximum flow is one-third, with many potentially having much weaker surface expressions. The Labrador Sea anticyclones, by contrast, typically have a current strength measured at 110 m that is one-half the maximum value.

The composite nature of the Labrador Sea anticyclones, most apparent in eddy F ([Fig. 5f](#) ) , is another important feature. Other observed SCVs tend to have a single well-defined  $\theta/S$  anomaly in the vertical. This is true for meddies ([Armi and Zenk 1984](#); [Hebert et al. 1990](#); [Pingree and LeCann 1993](#)) as well as others ([Elliott and Sanford 1986](#); [Riser et al. 1986](#); [D'Asaro et al. 1994](#)), with a notable exception being the double meddy observed by [Prater and Sanford \(1994\)](#). Such composite cores may be related to the evolution of baroclinic planetary turbulence into a more barotropic state; this effect is seen in layered models ([Rhines 1977](#)) as well as in three-dimensional models ([McWilliams et al. 1994](#)) of rotating stratified turbulence.

Despite the fact that anticyclonic eddy cores occur at depths between 500 m and 1500 m, from the point of view of a two-layer model they represent upper-layer potential vorticity anomalies. The dynamically important stratification to the first baroclinic mode is the thick deep pycnocline beneath 2 km, not the thin surface stratification. This is in contrast to many subtropical eddies, which tend to have PV anomalies within or beneath the main pycnocline.

## 6. Discussion

We identify a number of events observed at the Bravo mooring during June–November 1994 as advected eddies of two distinct types: two cyclones and four anticyclones. Warm cyclones appear to originate in the Irminger boundary current, while cold anticyclones are products of deep convection.

When compared with other known submesoscale eddies, the Labrador Sea anticyclones are characterized by their strong

barotropic modes and composite cores. Based on their Rossby numbers, the Labrador Sea anticyclones appear more closely related to meddies and hydrothermal megaplumes than to Arctic Ocean eddies.

The nature and statistics of the observed eddies are important for our understanding of deep convection. For instance, in numerical models of deep convection the baroclinic instability of a convected “chimney” leads to roughly equal numbers of cyclonic and anticyclonic eddies organized into rapidly propagating “hetons” (Legg and Marshall 1993; Send and Marshall 1995). Yet, of the six eddies we observed, none are convectively generated cyclones; events C and D originate in the boundary current and not in central Labrador Sea deep convection.

### Acknowledgments

Helpful and stimulating comments from the following people are gratefully acknowledged: Eric D'Asaro, Eric Kunze, Mitsuhiro Kawase, Charlie Eriksen, Knut Aagaard, Parker MacCready, Jody Klymak, and Mark Prater. The vertical mode MATLAB code was cheerfully supplied by Gabe Vecchi and Sebastian. Hydrographic data was taken during the spring 1994 cruise of the C.S.S. *Hudson*, with John Lazier as chief scientist. Support for J. Lilly from a NDSEG Graduate Student Fellowship was greatly appreciated.

---

### References

- Armi L., and W. Zenk, 1984: Large lenses of highly saline Mediterranean Water. *J. Phys. Oceanogr.*, **14**, 1560–1576. [Find this article online](#)
- Clarke R. A., and J.-C. Gascard, 1983: The formation of Labrador Sea Water. Part I: Large-scale processes. *J. Phys. Oceanogr.*, **13**, 1764–1778. [Find this article online](#)
- D'Asaro E. A., 1988: Generation of submesoscale vortices: A new mechanism. *J. Geophys. Res.*, **93**, 6685–6693, (C6). [Find this article online](#)
- D'Asaro E. A., S. Walker, and E. Baker, 1994: Structure of two hydrothermal megaplumes. *J. Geophys. Res.*, **99**, 20361–20373, (C10). [Find this article online](#)
- Elliott B., and T. Sanford, 1986: The subthermocline lens D1. Part I: Description of water properties and velocity profiles. *J. Phys. Oceanogr.*, **16**, 532–548. [Find this article online](#)
- Gascard J., 1978: Mediterranean deep water formation, baroclinic instability, and oceanic eddies. *Oceanol. Acta*, **1**, 315–330. [Find this article online](#)
- Gascard J., and R. A. Clarke, 1983: The formation of Labrador Sea Water. Part II: Mesoscale and smaller-scale processes. *J. Phys. Oceanogr.*, **13**, 1779–1797. [Find this article online](#)
- Häkkinen S., 1999: A simulation of the effects of a Great Salinity Anomaly. *J. Climate*, **12**, 1781–1795. [Find this article online](#)
- Hebert D., N. Oakey, and B. Ruddick, 1990: Evolution of a Mediterranean salt lens: Scalar properties. *J. Phys. Oceanogr.*, **20**, 1468–1483. [Find this article online](#)
- Jones H., and J. Marshall, 1997: Restratification after deep convection. *J. Phys. Oceanogr.*, **27**, 2276–2287. [Find this article online](#)
- Käse R. H., and W. Zenk, 1987: Reconstructed Mediterranean salt lens trajectories. *J. Phys. Oceanogr.*, **17**, 158–163. [Find this article online](#)
- Lazier J. R. N., 1973: The renewal of Labrador Sea Water. *Deep-Sea Res.*, **20**, 341–353. [Find this article online](#)
- Lazier J. R. N., 1980: Oceanographic conditions at Ocean Weather Ship *Bravo*, 1964–1974. *Atmos.–Ocean*, **18**, 227–238. [Find this article online](#)
- Legg S., and J. Marshall, 1993: A heton model of the spreading phase of open-ocean deep convection. *J. Phys. Oceanogr.*, **23**, 1040–1056. [Find this article online](#)
- Legg S., J. McWilliams, and J. Gao, 1998: Localization of deep ocean convection by a mesoscale eddy. *J. Phys. Oceanogr.*, **28**, 944–970. [Find this article online](#)
- Lilly J. M., P. B. Rhines, M. Visbeck, R. Davis, J. R. Lazier, F. Schott, and D. Farmer, 1999: Observing deep convection in the Labrador Sea during winter 1994/95. *J. Phys. Oceanogr.*, **29**, 2065–2098. [Find this article online](#)



Marshall J., and F. Schott, 1999: Open-ocean convection: Observations, theory and models. *Rev. Geophys.*, **37**, 1–64.

McWilliams J. C., 1988: Vortex generation through balanced adjustment. *J. Phys. Oceanogr.*, **18**, 1178–1192. [Find this article online](#)

McWilliams J. C., J. B. Weiss, and I. Yavneh, 1994: Anisotropy and coherent vortex structures in planetary turbulence. *Science*, **264**, 410–413. [Find this article online](#)

Pingree R., and B. LeCann, 1993: Structure of a Meddy (Bobby 92) southeast of the Azores. *Deep-Sea Res.*, **40**, 2077–2103. [Find this article online](#)

Prater M. D., and T. Sanford, 1994: A Meddy off Cape Vincent. Part I: Description. *J. Phys. Oceanogr.*, **24**, 1572–1586. [Find this article online](#)

Rhines P. B., 1977: The dynamics of unsteady currents. *The Sea*, E. Goldberg, Ed., *Marine Modeling*, Vol. 6, John Wiley and Sons, 189–318.

Riser S. C., W. B. Owens, H. T. Rossby, and C. C. Ebbesmeyer, 1986: The structure, dynamics, and origin of a small-scale lens of water in the western North Atlantic thermocline. *J. Phys. Oceanogr.*, **16**, 572–590. [Find this article online](#)

Send U., and J. Marshall, 1995: Integral effects of deep convection. *J. Phys. Oceanogr.*, **25**, 855–872. [Find this article online](#)

Stammer D., H.-H. Hinrichsen, and R. H. Käse, 1991: Can Meddies be detected by satellite altimetry? *J. Geophys. Res.*, **96**, 7005–7014, (C4). [Find this article online](#)

Straneo F., and M. Kawase, 1999: Comparisons of localized convection due to localized forcing and preconditioning. *J. Phys. Oceanogr.*, **29**, 55–68. [Find this article online](#)

Talley L., and M. McCartney, 1982: The distribution and circulation of Labrador Sea Water. *J. Phys. Oceanogr.*, **12**, 1189–1205. [Find this article online](#)

---

## APPENDIX

### 7. Estimating the Sizes and Strengths of Advected Eddies

We now define a set of measures used to characterize coherent eddies. The actual peak azimuthal velocity at any depth is  $V$ , the half-width or “apparent” radius is  $X$ , and the eddy is moving with a speed  $U$  in direction  $\Theta$ . We would like to form estimates of these quantities, denoted  $\tilde{V}$ ,  $\tilde{X}$ ,  $\tilde{U}$ , and  $\tilde{\Theta}$ .

The edges of an eddy's velocity core are expected to define a local maximum of the velocity difference between two points. Given initial guesses for the eddy's center  $t_o$  and half-duration  $\Delta T$ , refined values are found that maximize

$$\tilde{V}_n \equiv |\xi(t_o - \Delta T) - \xi(t_o + \Delta T)|,$$

where  $\xi$  is the complex velocity  $u + iv$ , over a window small enough to prevent interference from other eddies. Since we also expect the velocity signal to be largest in the direction perpendicular to the advecting flow, the advection direction ( $\pm 180^\circ$ ) can be estimated as  $\tilde{\Theta} = \arg\{\tilde{V}_n\} + \pi/2$ .

For a constant background flow advecting an azimuthally symmetric eddy,  $\tilde{V}_n$  will be the velocity component perpendicular to the advecting flow, which is equivalent to  $VXR^{-1}$  where  $R$  is the eddy radius and  $X$  is the half-width of the eddy chord intersected by the mooring. This measure is expected to underestimate the magnitude of the azimuthal velocity, but has the advantage that aliasing of the advecting flow is minimized.

A second measure of the eddy velocity can be formed by subtracting an estimate of the advecting flow,

$$\begin{aligned}\tilde{V}_U = & \frac{1}{2} |\xi(t_o - \Delta T) - \tilde{U}_w e^{i\tilde{\Theta}_w}| \\ & + \frac{1}{2} |\xi(t_o + \Delta T) - \tilde{U}_w e^{i\tilde{\Theta}_w}|,\end{aligned}$$

where the specific mean flow estimate  $\tilde{U}_w e^{i\tilde{\Theta}_w}$  is defined below.

The eddy polarity (cyclonic or anticyclonic) is found from the vertical structure of the speed together with the density structure. Note that  $\tilde{V}_n$  and  $\tilde{V}_U$  are adjusted to be positive for a cyclone and negative for an anticyclone.

If the advecting flow is large in magnitude relative to the eddy, and slowly varying relative to the eddy's duration, then the advecting flow can be estimated by low passing the time series. This estimate  $\tilde{U}_f e^{i\tilde{\Theta}_f}$  is defined as the low-passed filtered velocity times series  $u + iv$  at the eddy center  $t_0$ . The instrument level used corresponds to the eddy's maximum currents, and the filter is a Hanning window whose width is three times the width of the eddy core.

A second way to estimate the advection velocity is to compare the observed currents with the observed shear. For an equivalent barotropic eddy, the eddy currents will be everywhere parallel to the eddy vertical shear. However, the total currents will not be parallel to the observed shear, since the eddy currents are offset by the (presumably barotropic) advecting flow but the shear is not. Therefore, the estimate  $\tilde{U}_a e^{i\tilde{\Theta}_a}$  minimizes the angle difference

$$\Delta\Theta = |\arg\{\xi_{z_{\max}} - \tilde{U}_a e^{i\tilde{\Theta}_a}\} - \arg\{\xi_{z_{\max}} - \xi_{z_{\min}}\}| \quad (\text{A1})$$

over the time window encompassing the eddy, which we choose to be  $(t_0 - 2\Delta T, t_0 + 2\Delta T)$ . Here  $z_{\max}$  ( $z_{\min}$ ) is the depth at which the eddy currents are largest (smallest).

These two estimates of the advection flow lead to two corresponding estimates of the eddy size ( $\tilde{X}_f$  and  $\tilde{X}_a$ ) since  $U\Delta T = X$ . It should be emphasized that the apparent eddy size as observed from the mooring will tend to be smaller than the actual radius, since the eddies will generally be sliced off-center.

The resulting estimates are shown in [Table 2](#). Agreement between the two methods of estimating  $U$  is good except for eddy A, which is the longest-duration event. This is encouraging since these two methods are quite different. The two methods for estimating  $V$  also agree well, with only eddy E having a significant difference between the two methods.

## Tables

TABLE 1. Bravo mooring instrumentation 1994–95. Measurements are “t” for temperature, “c” for conductivity, “p” for pressure, “spd” for current speed, and “dir” for current direction

Depth (m)	Instrument	Measurement
110	Aanderaa RCM-8	spd, dir, t, p
260	SeaBird 16 SEACAT	t, c
510	SeaBird 16 SEACAT	t, c
760	Aanderaa RCM-8	spd, dir, t
1010	SeaBird 16 SEACAT	t, c, p
1260	Aanderaa RCM-8	spd, dir, t
1510	SeaBird 16 SEACAT	t, c
1760	Aanderaa RCM-8	spd, dir, t
2010	SeaBird 16 SEACAT	t, c
2510	SeaBird 16 SEACAT	t, c
3476	Aanderaa RCM-8	spd, dir, t

[Click on thumbnail for full-sized image.](#)

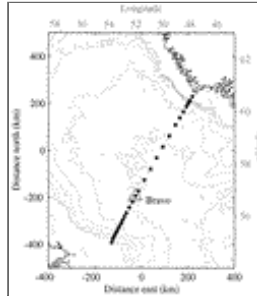
TABLE 2. Estimated eddy parameters:  $\Delta T$ : the temporal half-duration of an eddy,  $\hat{U}_a$  ( $\hat{X}_a$ ): the estimated mean flow speed (eddy apparent radius) using the “angle” method,  $\hat{U}_f$  ( $\hat{X}_f$ ): the estimated mean flow speed (eddy apparent radius) using the “filtering” method,  $\hat{V}_n$  ( $\hat{V}_U$ ): the estimated maximum eddy currents using the “normal” (“U subtraction”) method,  $\mathcal{R}$ : the range of

estimated Rossby numbers using the various values for  $V$  and  $X$ ,  $\Delta z$ : the potential difference between levels of maximum isopycnal displacement, and the  $\Delta\sigma$ : the eddy's maximum density anomaly. See text for details

	A	B	C	D	E	F
$\Delta z$ (m)	53	11.5	34.5	25	11.5	17
$V$ ( $\text{cm s}^{-1}$ )	6.5	12.7	11.8	12.6	11.8	8.6
$X$ (km)	12.5	17.7	11.6	19.4	18.7	7.7
$\Delta\sigma$ ( $\text{kg m}^{-3}$ )	11.9	5.2	10.7	11.3	5.4	5.2
$R$ (km)	23.8	7.3	14.4	15.4	7.8	4.7
$R$ ( $\text{cm s}^{-1}$ )	-17.2	-22.5	16.4	15.6	-6.1	-14.0
$R$ ( $\text{cm s}^{-1}$ )	-17.8	-13.0	16.4	17.0	-8.4	-14.0
$R$ (km)	0.15-0.24	0.27-0.40	0.18	0.15-0.24	0.17-0.25	0.44-0.49
$R$ (km)	1.25 - 0.25	1 - 0.25	1 - 0.25	1 - 0.25	1.5 - 0.25	1 - 0.25
$\text{Ro}(\text{Ro}^{-1})$	22 ± 1	12 ± 1	16 ± 1	38 ± 1	17 ± 1	9 ± 1

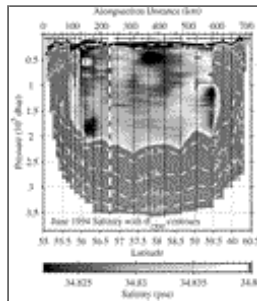
[Click on thumbnail for full-sized image.](#)

## Figures



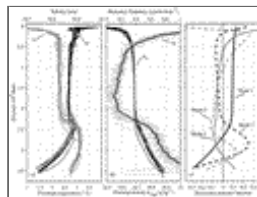
[Click on thumbnail for full-sized image.](#)

FIG. 1. Map of the Labrador Sea showing the location of the Bravo mooring (triangle) at  $56.75^\circ\text{N}$ ,  $52.5^\circ\text{W}$ . The station locations of the 1994 World Ocean Circulation Experiment (WOCE) AR7W hydrographic line are indicated by filled circles. The contour interval for the bathymetry (gray) is 500 m, the innermost contour intersected by the AR7W line being the 3500-m isobath



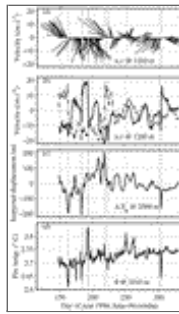
[Click on thumbnail for full-sized image.](#)

FIG. 2. A CTD section along the AR7W line between Labrador (left) and Greenland (right). Salinity is shown as shading, with a very narrow range emphasizing the freshest water in the interior. Contours of potential density  $\sigma_{1500}$  are also shown. Thin vertical lines denote the locations of CTD stations, and the location of the Bravo mooring is shown by a dashed white line



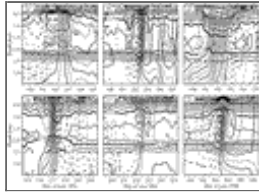
[Click on thumbnail for full-sized image.](#)

FIG. 3. The vertical structure of the interior Labrador Sea, from CTD casts during Jun 1994. (a) Potential temperature  $\theta$  (black) and salinity (gray). (b) Potential density  $\sigma_{1500}$  (black) and buoyancy frequency from vertically smoothed data (gray). The average of all the individual buoyancy frequency profiles is also shown. (c) The horizontal structure function from a modal decomposition (using the rigid-lid approximation) of section-averaged, 50-m decimated  $N^2$  profiles



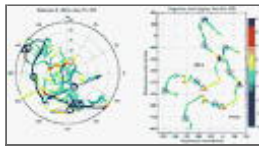
[Click on thumbnail for full-sized image.](#)

FIG. 4. Velocity transitions during the 6-month period Jun–Nov 1994. (a) Stick vectors at 1260 m with approximately one stick per day shown. The  $u$  and  $v$  time series shown here as well as all other time series data in this paper have been smoothed with a 24-h Hanning filter. Vertical lines mark the locations of sudden rotations of the velocity that are shown to be due to the advection of small-scale eddies. (b) Time series of  $u$  (solid) and  $v$  (dashed) at 1260 m. (c) Isopycnal displacement  $\Delta Z_\sigma$  at 2500 m. (d) Potential temperature  $\theta$  at 1010 m



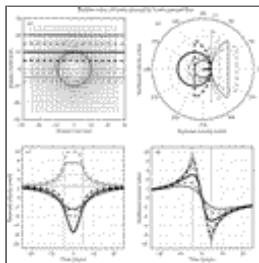
[Click on thumbnail for full-sized image.](#)

FIG. 5. Potential temperature  $\theta$  and normal velocity  $v_n$  cross sections through eddies A–F. Identical time windows and contours are used for each event. Black lines are contours of potential temperature, measured at 11 instruments. The contour interval is  $0.01^\circ\text{C}$  with labeling every  $0.05^\circ\text{C}$ . Gray lines are contours of normal velocity  $v_n$  (measured at six instruments) every  $2\text{ cm s}^{-1}$  with labeling every  $4\text{ cm s}^{-1}$ ; negative contours are dashed. Normal velocity is negative for early times for advected anticyclones (A, B, E, F) and positive for advected cyclones (C, D)



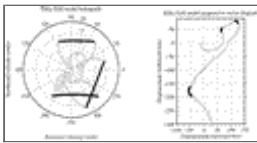
[Click on thumbnail for full-sized image.](#)

FIG. 6. (a) Hodograph of the currents observed at 1260 m for the time period Jun–Dec. Color denotes potential temperature at 1010 m, detrended over this time period to remove a slow warming. Six events that resemble advected eddies have been marked. The estimated centers of these events have been marked with circles (cold anticyclones) and triangles (warm cyclones). (b) Progressive vector diagram for 1260 m (upper curve) as well as for 3476 m (lower curve). Color is the same as for (a)



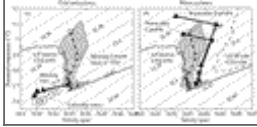
[Click on thumbnail for full-sized image.](#)

FIG. 7. An advected cyclonic model eddy “sliced” by an array of moorings. (a) The eddy currents in plan view in the reference frame moving with the eddy. The maximum speed, at the eddy rim (gray circle), is  $10\text{ cm s}^{-1}$ . Horizontal lines are the paths the moorings take through the eddy, with black and gray lines denoting trajectories passing on opposite sides of the eddy core. (b, c, d) The currents observed at each of the eight moorings as the eddy is advected past them. (b) Hodographs of the observed currents, with the advecting flow ( $2.5\text{ cm s}^{-1}$  to the east) shown by an arrow. (c) Eastward, or parallel, component of the velocity. The eddy rim for a slice through the exact center is marked with vertical lines in this and the following plot. (d) Northward, or perpendicular, velocity component.



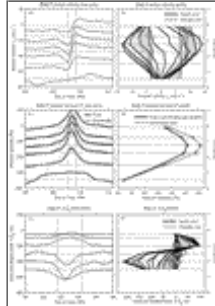
Click on thumbnail for full-sized image.

FIG. 8. (a) Hodograph from a realization of an idealized eddy-field model. In this model, at time  $t_0$  64 Rankine vortices are located on a regular grid plus a small random perturbation. The eddies have  $|5 + G|$  km radius, where  $G$  is a unit variance Gaussian random variable, and maximum azimuthal currents of random sign and magnitude  $10 + 2.5G$  cm s<sup>-1</sup>. The initial spacing is 50 km in both  $x$  and  $y$  directions, and each eddy's center is perturbed by  $12.5G$  km in both directions. The eddy field is integrated in time with a time step of 1 h for 2048 hours in the forward and reverse directions from  $t = t_0$ , with each eddy being advected by the total velocity at its exact center. The hodograph is from a mooring at the center of the eddy grid. Black dots denote times when the mooring is inside an eddy's core; gray dots denote other times. (b) The progressive vector diagram for the time series whose hodograph is shown in (a)



Click on thumbnail for full-sized image.

FIG. 9. Potential temperature/salinity diagrams for (a) the cold anticyclones and (b) the warm cyclones, with  $\sigma_{1500}$  contours (contour interval of  $0.01$  g kg<sup>-1</sup>). In both panels, the mooring Jun–Nov mean is shown as a thick dashed black line marked by circles, and the shaded region represents the mean plus or minus one standard deviation. The black line is the mean May–Jun 1994 CTD profiles along the WOCE AR7W line for water depths greater than about 2200 m. In (a), the  $\theta/S$  properties of the eddy cores at 1010 m are given by circled letters. The thick black line marked by triangles is the mean mooring profile for Mar 1995. In (b), the thin dashed black line is the mean CTD profile from the Irminger boundary current on the Greenland side of the Labrador Basin. The mooring profiles through the two warm eddies for the upper four instruments are shown with thick black lines marked by squares (eddy C) or triangles (eddy D). Mooring instrument depths are 260, 510, 1010, 1510, 2010, and 2512 m, with the lowest depth omitted except for the mean profiles



Click on thumbnail for full-sized image.

FIG. 10. Details of eddy F. (a, c, e) Time series, offset by an amount proportional to the depth spacing between instruments. Vertical gray lines mark the edge of the velocity core, and horizontal gray lines mark the depths of measurements. Note that (a) and (c) have wider time axes than (e). (b, d, f) Vertical profiles, and the vertical gray lines mark the locations of the normal velocity extrema. Horizontal lines again mark the depths of measurements. In (b) and (f), profiles are shown every 4 h, and thick (thin) lines are for times inside (outside) the eddy core. (a) and (b) The normal velocity  $\mathbf{v}_n$  through the eddy. The perturbation pressure inferred from the velocity data is shown in (c) and (d). The contribution of the geostrophic term  $f\mathbf{v}$  is the thin line, and the total ( $f\mathbf{v} + \mathbf{v}^2 r^{-1}$ ) is the thick line. Profiles in (d) are through the center of the eddy. The isopycnal displacement  $\Delta Z_\sigma$  is shown in (e) and (f)

<sup>1</sup> Note that this composite structure is not an artifact of interleaving two different kinds of temperature instruments (Aanderaas and SEACATs) with drastically different accuracy. The cores and the breaks between them are all observed by the SEACATs.





© 2008 American Meteorological Society [Privacy Policy and Disclaimer](#)  
Headquarters: 45 Beacon Street Boston, MA 02108-3693  
DC Office: 1120 G Street, NW, Suite 800 Washington DC, 20005-3826  
[amsinfo@ametsoc.org](mailto:amsinfo@ametsoc.org) Phone: 617-227-2425 Fax: 617-742-8718  
[Allen Press, Inc.](#) assists in the online publication of *AMS* journals.